Densification and microstructure development in spark plasma sintered WC–6 wt% ZrO_2 nanocomposites

Krishanu Biswas
Department of Materials Engineering, Indian Institute of Science, Bangalore, India

Amartya Mukhopadhyay and Bikramjit Basu[a)]
Laboratory for Advanced Ceramics, Department of Materials and Metallurgical Engineering, Indian Institute of Technology, Kanpur, India

Kamanio Chattopadhyay
Department of Materials Engineering, Indian Institute of Science, Bangalore, India

(Received 31 May 2006; accepted 6 December 2006)

In this paper, we report the results of a transmission electron microscopy investigation on WC–6 wt% ZrO_2 nanocomposite, spark plasma sintered at 1300 °C, for varying times of up to 20 min. The primary aim of this work was to understand the evolution of microstructure during such a sintering process. The investigation revealed the presence of nanocrystalline ZrO_2 particles (30–50 nm) entrapped within submicron WC grains. In addition, relatively coarser ZrO_2 (60–100 nm) particles were observed to be either attached to WC grain boundaries or located at WC triple grain junctions. The evidence of the presence of a small amount of W_2C, supposed to have been formed due to sintering reaction between WC and ZrO_2, is presented here. Detailed structural investigation indicated that ZrO_2 in the spark plasma sintered nanocomposite adopted an orthorhombic crystal structure, and the possible reasons for o-ZrO_2 formation are explained. The increase in kinetics of densification due to the addition of ZrO_2 is believed to be caused by the enhanced diffusion kinetics in the presence of nonstoichiometric nanocrystalline ZrO_2.

I. INTRODUCTION

The potential of nanostructured materials—in particular ceramic nanocomposites—to realize improved as well as novel properties with respect to the conventional materials has inspired significant research activities on the synthesis of nanoceramic composites in technologically important ceramic systems.[1–8] These nanocomposites can be broadly classified into two categories[9]: (i) nanocomposites, fabricated by dispersion of nanosized particles within micron-sized matrix grains or at the grain boundaries of the matrix, and (ii) nano/nanocomposites, in which matrix grains are also on the nano-sized scale.

A major difficulty for the synthesis of nanocomposites is the grain growth during sintering. The adoption of "activated sintering," which involves a combination of much lower sintering temperature and shorter sintering time, has been reported to be successful in synthesizing nanocomposites.[10–15] In particular, the advent of field-activated sintering techniques (FAST) has enabled the fabrication of ceramic nanocomposites. This technique involves the application of pulsed electrical field in combination with resistance heating and pressure to achieve high heating rates and fast sintering of powders (with minimum grain coarsening). Electric field during sintering produces electric discharges and possibly plasma at the void spaces between powder particles.[16,17] A considerable amount of research has been directed toward the development of ceramic nanocomposites using the spark plasma sintering (SPS) technique, a variant of FAST techniques.[10–15]

In our recent research efforts to develop nanocomposites, WC-based ceramic composites using ZrO_2 sinter-additive were developed using the SPS technique. It was observed that pressureless sintering at 1700 °C for 1 h or SPS at 1300 °C for 5 min can yield near theoretical densification in the WC–6 wt% ZrO_2 materials.[1,18] The mechanical[1,18] and tribological properties[19] of these newly developed ceramic composites and nanocomposites have been investigated. The experimental measurements have indicated that a combination of high hardness (up to 24 GPa) and moderate fracture toughness (~5 MPa $m^{1/2}$) is obtainable in spark sintered WC–6 wt% ZrO_2.[1] Additionally, high wear resistance (wear rate ~10^{-8} mm^3/N m)

[a)]Address all correspondence to this author.
e-mail: bikram@iitk.ac.in
DOI: 10.1557/JMR.2007.0189

against bearing steel has also been measured for the spark sintered composites.[19]

The present paper reports detailed transmission electron microscope (TEM) characterization of WC–6 wt% ZrO_2 composite to present the microstructural evolution and analyze the stabilization of ZrO_2 as well as the formation or absence of any reaction product. On the basis of these results, we shall aim at developing insights into the process of densification and the microstructural evolution during the sintering process.

II. EXPERIMENTAL PROCEDURE

A. Processing

Commercial purity WC powder (average particle size 0.2 μm, H.C. Starck, Germany) was used for the matrix in the composites. The average particle size of the starting zirconia powders (Tosoh grade, Tosoh corporation, Tokyo, Japan) was 27 nm, and the major impurities included Al_2O_3 (<0.005 wt%) and SiO_2 (0.007 wt%). The starting powders of 50–75 g, with a WC:ZrO_2 weight ratio of 94:6, were mixed for 24 h in 1 l *n*-propanol in a polyethylene bottle. To break the agglomerates, WC balls were used during the mixing process. After mixing, the propanol was removed by means of a rotating evaporator. The dried powder mixture was placed into a cylindrical graphite die 10 mm in diameter. During the SPS experiments, the graphite die-punch assembly was placed inside the SPS chamber (Eltech Co., Ulsan, Korea) between two graphite electrodes. The sintering experiments were carried out under a vacuum of 50–60 mTorr at different temperatures in the range of 1200–1400 °C under a pressure of 30 MPa. A high current on the order of 1–1.2 kA was passed between the graphite electrodes. The desired sintering temperature was reached within 2 min of processing time. This resulted in a high heating rate on the order of 600 K/min. The process was terminated, and the pressure was released after it was held at the sintering temperature for times varying in the range of 2–20 min.

B. Characterization

The densities of all the specimens, prepared by varying the holding time, were measured using distilled water as the medium, according to the Archimedes method. To identify different phases, x-ray diffraction (XRD) patterns were obtained using an x-ray diffractometer (JEOL JDX 8030) with Cu K_α radiation ($\lambda = 0.154$ nm). In general, XRD data were collected at a scan rate of 1°/min. For more critical analysis of ZrO_2 structure, additional data were obtained at a slower scan rate of 0.1°/min in the 2θ range of 47–51°. Detailed microstructural analysis of the samples, prepared at the different sintering conditions (SPS at 1300 °C for 5 and 20 min), was performed using TEM (JEOL 2000 FXII operated at 200 kV and Technai G^2 operated at 300 kV). Energy dispersive (EDS) spectra were also obtained from selected areas during observation in TEM. Electron transparent thin foils for TEM observation were prepared by the standard preparation technique, which includes cutting of 3-mm disks, grinding, dimpling, and subsequent ion-milling using argon gas ions at 5 kV at an angle of 15° until perforation occurred.

III. RESULTS

A. Phase assemblage identification by XRD

XRD investigation of starting powder and spark plasma sintered samples for different sintering times [see Fig. 1(a)] indicated the presence of ZrO_2 and hexagonal WC ($a = 0.291$, $c = 0.284$ nm) as major phases in all the spark plasma sintered samples. The presence of hexagonal α–W_2C ($a = 0.519$ nm and $c = 0.472$ nm) was detected in samples sintered for 5 min or more. ZrO_2 peaks in the diffraction patterns could be consistently indexed using orthorhombic (o-ZrO_2) structure ($a = 0.5068$ nm, $b = 0.526$ nm, and $c = 0.5077$ nm) with space group $Pbc2_1$. The structure of o-ZrO_2 is closely related to the crystal structure of tetragonal zirconia (t-ZrO_2)[20] and is thus difficult to distinguish.[21] To clarify the structure of ZrO_2 in the spark plasma sintered composite (1300 °C, 5 min), XRD patterns were recorded at a slower scan rate (0.1°/min) in the 2θ range of 47° to 51°, where {220} type peaks of ZrO_2 appeared [Fig. 1(b)]. The XRD pattern, obtained from starting powder (not shown here), showed the presence of (220) and (202) peaks, indicating tetragonal structure of ZrO_2 in the starting powder. However, XRD patterns, recorded from spark plasma sintered samples, revealed that the {220} peak of ZrO_2 split into three characteristic and distinguishable peaks, which could be indexed as (022), (220), and (202) peaks. The presence of the extra peak (022) (compared with the XRD pattern of starting powder) indicated that ZrO_2 in the spark plasma sintered sample adopted the orthorhombic structure. The black lines in Fig. 1(b) indicate the location of ZrO_2 peaks, as described by JCPDS-ICDD (Joint Committee for Powder Diffraction Studies–International Center for Diffraction Data) data file Card No: 79-1796. This distinctive feature to identify o-ZrO_2 from t-ZrO_2 has been discussed in the literature.[20,21] Further, no evidence of monoclinic ZrO_2 was found in the spark plasma sintered samples. This suggests that the orthorhombic phase of ZrO_2 was stabilized and its transformation to monoclinic ZrO_2 did not occur during cooling from sintering temperature. In the present case, o-ZrO_2 appeared to have been produced by solid-state transformation of t-ZrO_2 during SPS processing. The occurrence of o-ZrO_2 was frequently observed during other investigations concerning TEM studies of thin foils of partially stabilized t-ZrO_2.

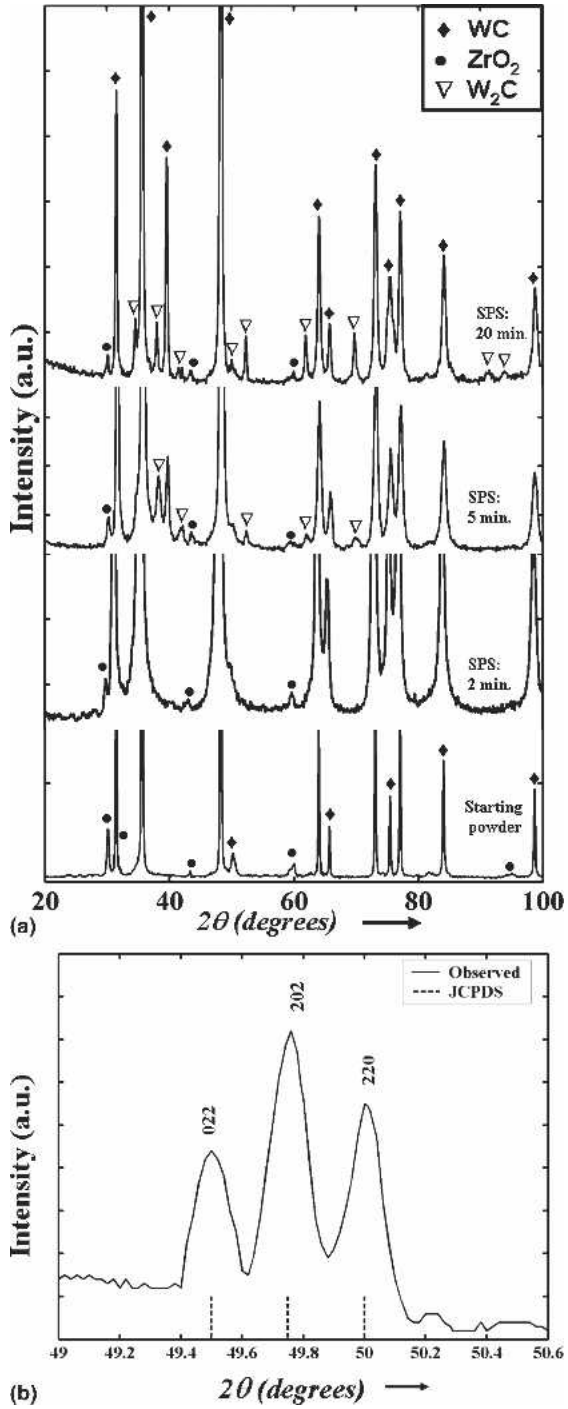

FIG. 1. (a) XRD patterns of starting powder and sintered samples of WC–6 wt% ZrO_2, spark plasma sintered at 1300 °C for varying times up to 20 min and (b) slow scan (0.1°/min) XRD pattern from samples processed for 5 min showing splitting of {220} peak of ZrO_2, indicating orthorhombic structure of ZrO_2.

However, Marshall et al.[22] reported that the t-ZrO_2 to o-ZrO_2 transformation occurs throughout the bulk of the specimen using the neutron diffraction technique. More definitive proof of the presence of o-ZrO_2 is presented in Sec. III. C.

Additionally, a detectable amount of W_2C was observed to form when spark sintering was carried out for 5 min or more [Fig. 1(a)]. Because only WC and ZrO_2 were detected in the starting powders [Fig. 1(a)], the W_2C formation must have been the result of sintering reaction between WC and ZrO_2. The possible reaction pathway for W_2C formation will be discussed in Sec. IV.

B. Densification

In Table I, the sintering conditions as well as the sinter densities (also percent densification) of spark plasma sintered WC-based nanocomposites are presented. It must be mentioned here that the theoretical densities of the WC–6 wt% ZrO_2 composites (SPS; 2, 5, 20 min) were calculated according to rule of mixture, assuming theoretical densities of 15.3, 17.2, and 6.2 gm/cc for WC, W_2C, and ZrO_2, respectively. The estimation of the amounts of W_2C (vol%), after spark sintering for the different holding periods (2–20 min), was made by measuring the areas under the characteristic XRD peaks of W_2C (see Sec. III. A) and subsequently dividing them by the area under all the x-ray peaks.

The density data revealed that near-theoretical densification (over 99% theoretical density) can be achieved for the WC–6 wt% ZrO_2 (3Y) nanocomposites via spark sintering at a relatively lower temperature of 1300 °C with holding times of 5 min or higher. As a reference, the literature data for binderless WC[20] are also included in Table I. It should be noted that incorporation of nanocrystalline ZrO_2 significantly reduces the sintering temperature required for achieving near-theoretical densification of WC from 1700 °C (binderless WC[20]) to 1300 °C (WC–6 wt% ZrO_2) when WC is sintered via the same consolidation technique. Because Co has been widely used as a binder phase in densifying WC–Co cemented carbides, additional SPS experiments were carried out on WC–6 wt% Co cemented carbides,[1] and the density data from these samples are also presented in Table I for comparison. Additionally, the density data of WC–6 wt% ZrO_2 composites processed by pressureless sintering, as reported in one of our recent papers,[18] are included in Table I.

Critical inspection of the data presented in Table I reveal that WC can be sintered using ZrO_2 as an additive at a temperature (1300 °C) lower than that required when Co is used as the binder (1400 °C) in the SPS route. Therefore, ZrO_2, as an alternative to Co binder, can be effectively used as a sinter-additive for achieving better densification of WC composites. The effectiveness of SPS over pressureless sintering can be illustrated from the fact that full densification of the same composite composition (WC–6 wt% ZrO_2) via spark plasma sintering takes place at a temperature 400 °C lower than that required for pressureless sintering (1700 °C). In addition to a lower sintering temperature, holding time of only

TABLE I. Densification data of WC–6 wt% ZrO_2 composites and WC–6 wt% Co cemented carbides sintered via spark plasma sintering (SPS) and pressureless sintering (PS) in vacuum.

Material composition	Sintering techniques and temperatures (°C)	Holding times (min)	vol% W_2C	ρ (gm/cc)	% ρ_{th}	References
WC	SPS, 1700	0	…	…	98.0	20
WC–6 wt% ZrO_2 (3Y)	SPS, 1300	2	0	11.6	81.2	present
WC–6 wt% ZrO_2 (3Y)	SPS, 1300	5	5.1	14.3	99.9	present
WC–6 wt% ZrO_2 (3Y)	PS, 1300	20	7.6	14.2	99.4	present
WC–6 wt% ZrO_2 (3Y)	SPS, 1700	60	…	14.2	99.5	18
WC–6 wt% Co	SPS, 1300	5	…	13.6	91.4	1
WC–6 wt% Co	SPS, 1400	5	…	15.1	100	1

5 min is required for SPS, in contrast to the time of 1 h needed for pressureless sintering, which further elucidates the occurrence of rapid densification via the SPS route.

It can be noted that densification of binderless WC, which was not feasible by conventional sintering techniques, can be achieved via the SPS route.[23,24] The data in Table I illustrate that the use of ZrO_2 as a sintering additive results in significant lowering of spark sintering temperature for full densification of WC. The possible reasons for significant enhancement of densification on incorporation of ZrO_2 will be discussed in Sec. IV.

C. TEM observations

A representative lower magnification TEM image [Fig. 2(a)] of the sample, spark plasma sintered for 5 min, revealed an overall fine microstructure with WC grains varying in the range of 0.3–0.5 μm along with ZrO_2 particles. The ZrO_2 particles are indicated in the figure by black arrows. Almost all of the observable WC grains were equiaxed in shape, and no abnormal grain growth of WC was noticed in the spark plasma sintered microstructure. Energy dispersive x-ray spectroscopy (EDS) analysis from different microstructural regions (not shown) confirmed the presence of both ZrO_2 and WC matrix. Higher magnification TEM images are presented in Figs. 2(b)–2(d) to illustrate the distribution of ZrO_2 particles in WC matrix. The insets of Figs. 2(b) and 2(c) show the microdiffraction patterns, which further confirmed the presence of WC grains. The presence of ZrO_2 particulates, 60–90 nm in size, was recorded at WC triple

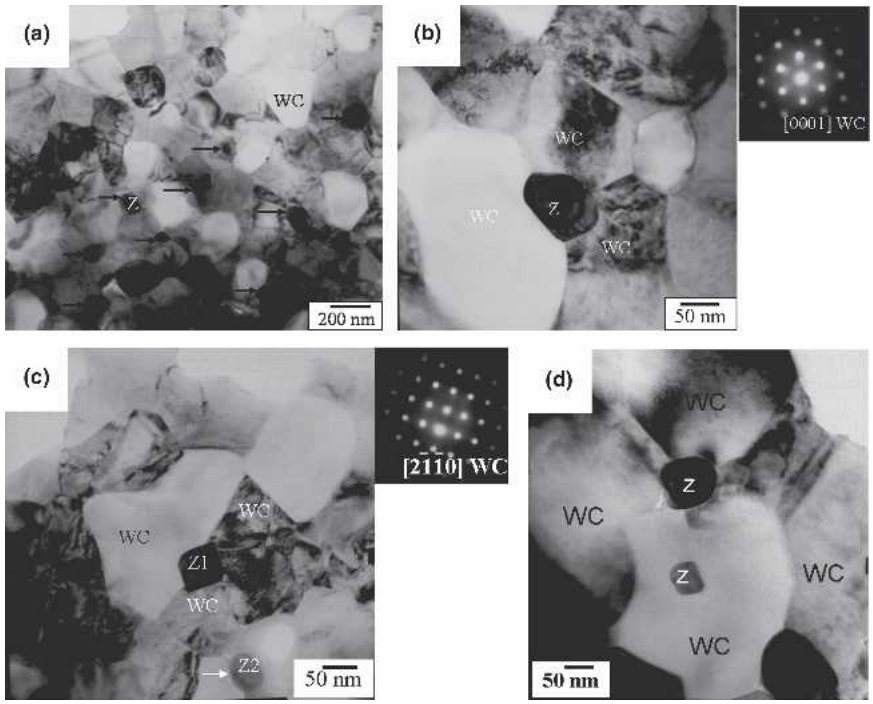

FIG. 2. (a) Low magnification bright-field image of WC-ZrO_2 nanocomposite (spark plasma sintered for 5 min at 1300 °C) showing distribution of nanocrystalline ZrO_2 particles (indicated by arrows) in submicron WC matrix. ZrO_2 particles are distributed in the WC matrix at (b) the triple junction, (c) the triple junction (Z1) and at the grain boundary (Z2), and (d) interior of a WC grain. The insets in (b) and (c) show microdiffraction patterns obtained from WC grains. (Z stands for ZrO_2)

junctions and grain boundaries [Figs. 2(b) and 2(c)]. One of the characteristic features of these nano-sized ZrO_2 particles is the faceted morphology. This morphology of ZrO_2 particles is prominent in Fig. 2(c). In contrast, much finer ZrO_2 particles (~30 nm) were found inside WC grains, as shown in Fig. 2(d). Considering the average grain sizes of the starting powders, 27 nm for ZrO_2 and 0.2 μm for WC, the above observations certainly indicate that limited grain growth occurred during spark sintering and thus resulted in the development of a nanocomposite microstructure.

To confirm the crystal structure of ZrO_2, a number of microdiffraction patterns were acquired and analyzed. An example of such analysis is shown in Fig. 3. The microdiffraction patterns can be consistently indexed in terms of orthorhombic ZrO_2 (a = 0.5068 nm, b = 0.526 nm, and c = 0.5077 nm). Low-intensity {100} and {112} diffraction spots of the orthorhombic phase are also observable. It is important to note that these reflections are forbidden in the tetragonal lattice and that monoclinic (m-ZrO_2) phase does not have reflections, corresponding to these interplanar spacing.[25] Additionally, the observations presented here were in good agreement with o-ZrO_2 structure, as reported by Kisi et al.[25] and Guinebretiere et al.[26] These observations, in combination with XRD results, reconfirmed the presence of o-ZrO_2 in the spark plasma sintered WC-ZrO_2 nanocomposite.

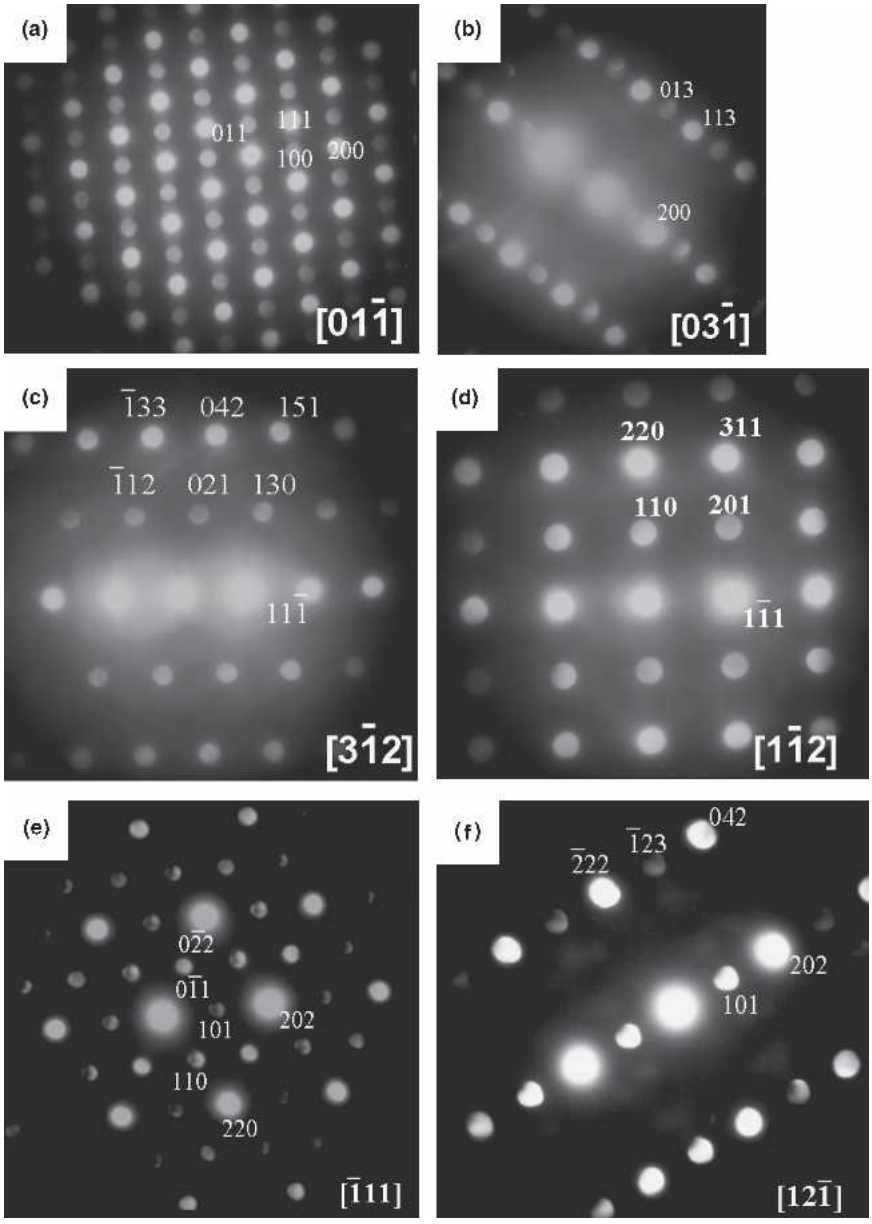

FIG. 3. A set of microdiffraction patterns obtained from nano-sized ZrO_2 particles, indicating orthorhombic structure of ZrO_2 in spark plasma sintered WC-ZrO_2 nanocomposite.

On closer observation [Fig. 4(a)], defect substructure was detected close to the WC/ZrO_2 interfaces or in the WC grains containing the nanocrystalline ZrO_2 particles. A very common characteristic of WC grains in the sample spark plasma sintered for 5 min was the presence of a large number of small angle boundaries. Figure 4(b) is a bright-field image, revealing a number of WC grains containing low angle boundaries (some of the grains marked as WC). The dark-field image (as shown in the inset) obtained using the $(10\bar{1}0)$ reflection of WC highlights one such boundary. The observation of defect substructure can be explained on the basis of residual stress. The coefficient of thermal expansion mismatch between WC and ZrO_2 ($\alpha_{TZP} = 11 \times 10^{-6}$ K^{-1} and $\alpha_{WC} = 5.2 \times 10^{-6}$ K^{-1}) can lead to an appreciable level of residual stresses during cooling from the sintering temperature.[27] To accommodate the residual stresses, i.e., to release the residual strain, defect substructures are therefore expected to form within the WC grains near the WC/ZrO_2 interfaces.

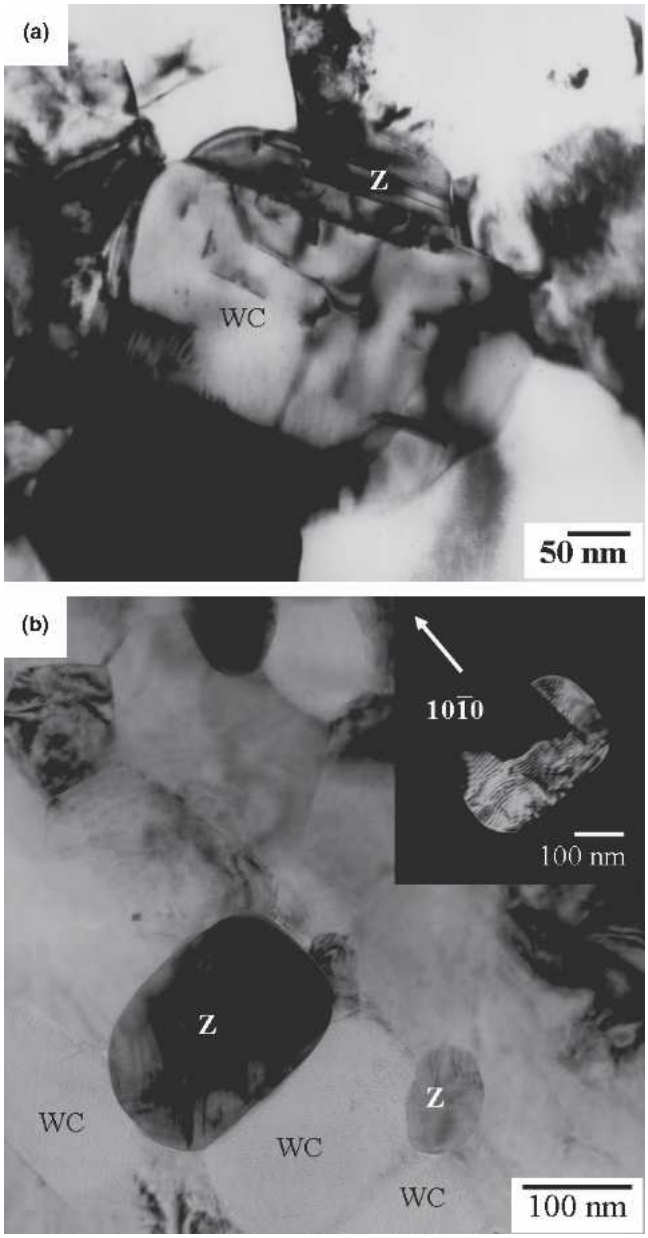

FIG. 4. Bright-field images showing defect structure inside WC grains: (a) a number of dislocations as observed inside a WC grain and (b) the presence of small angle grain boundaries with inset showing dark-field image of WC grain. (Z stands for ZrO_2)

Figure 5 shows a high-resolution image of two WC grains and the interface between them. The presence of atomically smooth grain boundary is an indication of good grain-to-grain bonding in spark sintered WC nanocomposites. This may be ascribed to the use of high-purity ceramic powders, the cleaning effect of electric discharge on the WC particle surface, and the thermal and electrical breakdown of insulating films on ceramic particles, which are inherent in SPS.[16]

The formation of α–W_2C was observed during TEM investigation for samples spark plasma sintered for 5 and 20 min. A typical bright-field image, depicting the presence of α–W_2C is shown in Fig. 6(a). Most of the observable α–W_2C grains were detected to be present between the o-ZrO_2 and WC grains. The microdiffraction pattern [Fig. 6(b)] obtained from such grains can be indexed using characteristic reflections of α–W_2C.

A representative bright-field micrograph of the composite, densified with a holding time of 20 min is shown in Fig. 7. Most of the WC grain sizes were around 0.4–0.5 μm. This observation indicated that the grain growth was restricted even on sintering for 20 min via the SPS process. This is in contrast to Omori,[24] who observed abnormal grain growth (about 1 mm grain size) of binderless WC on holding for just over 1 min, albeit at a much higher spark sintering temperature of 1900 °C. Observation of our spark sintered WC-ZrO_2 nanocomposite samples also showed that abnormal grain growth of WC was restricted considerably in contrast to the observation (on binderless WC) of Cha et al.[23] Therefore, ZrO_2 particles, located at the grain boundaries and triple junctions of WC grains, are effective in inhibiting grain growth, even after longer holding times. The WC grains in this sample contained a large number of planar defects, such as stacking faults and twins. The inset of Fig. 7 shows such a WC grain with defect structure (some of these marked by white arrows). Additionally, the formation of α–W_2C at the boundary between WC and ZrO_2 was also observed in this sample.

IV. DISCUSSION

The results obtained in this investigation indicate that nanocrystalline ZrO_2 is an effective sinter-additive in producing dense WC-ZrO_2 nanocomposite by the SPS

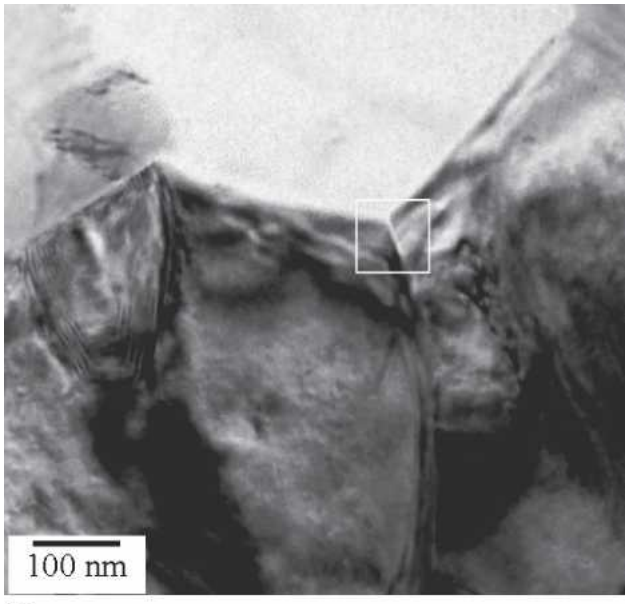

(a)

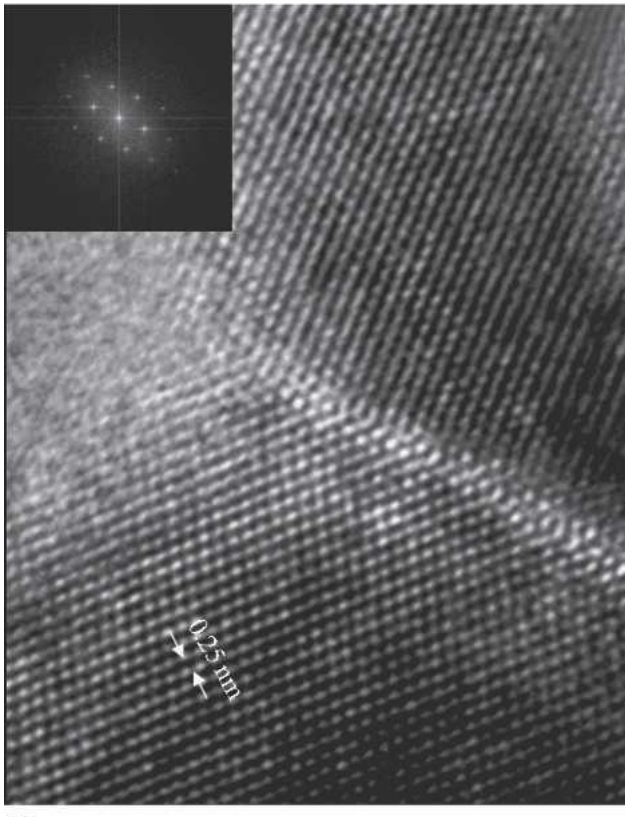

(b)

FIG. 5. (a) Bright-field micrograph showing the grain boundary between two WC grains and (b) high-resolution micrograph revealing atomically clean interface between the WC grains.

technique. We will first discuss the evolution of the microstructure, which will allow us to develop insight into the sintering process. ZrO_2 particles are mainly located at the grain boundaries and triple junctions of WC grains. No agglomeration of ZrO_2 particles has been observed; rather ZrO_2 particles are uniformly dispersed throughout the matrix. Both WC and ZrO_2 grains retain their fine size even after 20 min of spark sintering, indicating the fact that nano-sized ZrO_2 effectively inhibit the WC grain growth. This effect is similar to the results obtained for ZrO_2-WC composite, where WC is present only in a small amount.[28] Observations of ZrO_2 in the grain interior and triple points of WC indicate considerable interaction during the sintering process between ZrO_2 and WC particles. The presence of W_2C near the ZrO_2–WC interface has been conclusively established through TEM analysis. However, no evidence of elemental W could be found. The presence of elemental W was detected in earlier studies on a similar system.[27,28]

In the present work, the development of such fine-scaled microstructure in the WC-ZrO_2 nanocomposite can also be attributed to the high heating rate (600 °C/min) and lower sintering temperature (1300 °C). Because of the high heating rate, the final sintering temperature can be reached in less time. This implies that nondensifying mechanisms (such as surface diffusion), which are active at low temperature regime, can be suppressed. A direct consequence of this is the suppression of grain precoarsening before the final stage of sintering.

One of the important results of the structural characterization is the establishment of the presence of orthorhombic ZrO_2 phase with the lattice parameters of $a = 0.5068$ nm, $b = 0.526$ nm, and $c = 0.5077$ nm. The evidence of the presence of this phase exists in both the XRD patterns and electron diffraction patterns. The formation and crystal structure of o-ZrO_2 have been extensively studied in the literature.[20,21] This phase has been reported to form by quenching from high temperature (400 to 600 °C) and pressure (>3 to 4 GPa).[20,21] The t-ZrO_2 to o-ZrO_2 transformation also occurs below −100 °C during cooling from high temperature.[21] Once formed, the o-ZrO_2 phase has metastable existence at higher temperature (up to 400 °C). Heating to 400 °C causes the reverse transformation of the orthorhombic to tetragonal structure.[21] The orthorhombic phase of ZrO_2 has been observed by TEM in thin foils of several transformation toughened ZrO_2 ceramics.[29]

Because the starting powder contains only tetragonal ZrO_2, the evidence (XRD result) of orthorhombic ZrO_2 in as-sintered samples is related to the SPS process. It must be determined whether transformation is complete during the process of sintering or both the polymorphs coexist in spark plasma sintered samples. The XRD patterns, obtained from samples spark sintered for 5 and 20 min, allow for a qualitative estimate of whether the t-ZrO_2 to o-ZrO_2 is complete or o-ZrO_2 and t-ZrO_2 coexist. This has been carried out by comparing the intensities of (022), (220), and (202) peaks of o-ZrO_2 with that of t-ZrO_2.[21] The observed intensity ratio of I_O^{220}:I_T^{220},

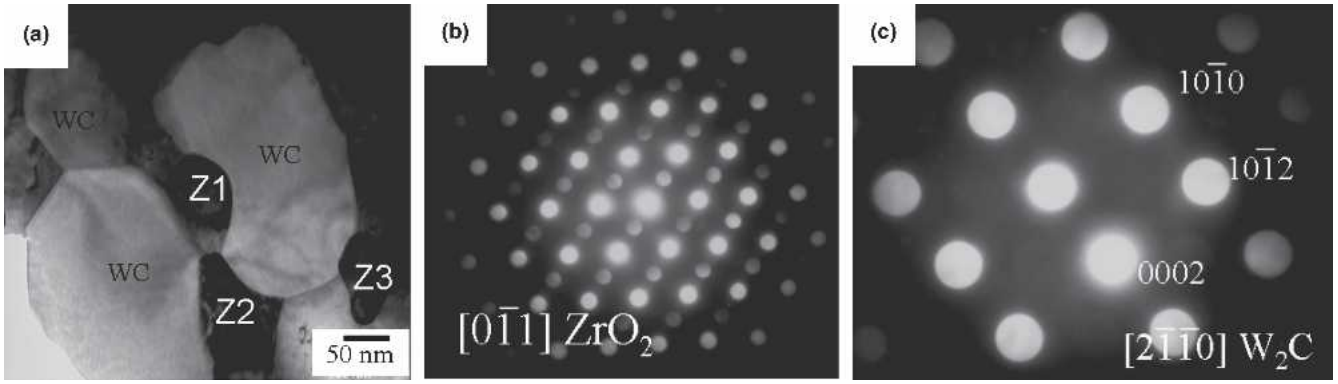

FIG. 6. (a) Bright-field TEM micrograph showing the presence of α-W_2C. The microdiffraction patterns as obtained from (b) ZrO_2 and (c) α–W_2C are also shown. (Z stands for ZrO_2)

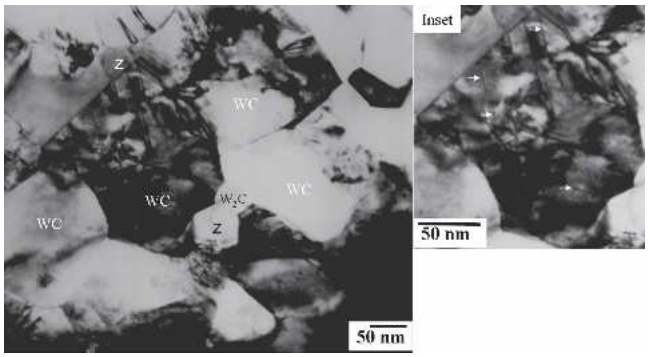

FIG. 7. Bright-field TEM micrograph of WC–6 wt% ZrO_2 nanocomposite, spark plasma sintered sample for 20 min, with inset showing a higher magnification micrograph of one WC containing a large number of defects (indicated by arrows).

in the present investigation, suggests that the latter is also present in the spark plasma sintered samples.

It must be noted here there is no evidence that the spark plasma process yields large pressure at high temperature, which can explain t-ZrO_2 to o-ZrO_2 transformation. Furthermore, the transformation at subzero temperature is ruled out in the present case as the samples have not experienced temperature lower than room temperature. Thus, the origin of o-ZrO_2 phase needs to be explained in terms of the constraining effect of the matrix as well as small size (nanocrystalline) of the ZrO_2 particles. If one considers the surrounding WC matrix as a rigid wall, the pressure that develops in ZrO_2 grains (during the high temperature exposure) due to mismatch of linear thermal expansion coefficient can be estimated using the following expression[30]:

$$\Delta P = \frac{[12(\alpha_{ZrO_2} - \alpha_{WC})\cdot\Delta T\cdot\mu_{WC}\cdot K_{ZrO_2}]}{(3K_{ZrO_2} + 4\ \mu_{WC})} \quad , \qquad (1)$$

where α is the linear thermal expansion coefficients, ΔT is the temperature difference, μ_{WC} is the shear modulus of WC, and K_{ZrO_2} is the bulk modulus of ZrO_2. The parameters used in the calculation are shown in Table II. The calculated pressure is found to be 2.55 GPa, which is somewhat less than that reported to be necessary (3–4 GPa) for the t- to o-ZrO_2 transformation.[20,21]

Additionally, the presence of the high pressure modification of ZrO_2 can also be partly explained on the basis of Gibbs–Thomson (GT) effect. According to GT effect, a hydrostatic pressure (Δp) develops inside a particle/crystallite, which is related to the surface energy (γ) and particle/crystallite diameter (d):

$$\Delta p = 4\gamma/d \quad . \qquad (2)$$

Considering the small (nanocrystalline) size, it is quite obvious that such an effect contributes considerably to the net pressure developed within the ZrO_2 particles. Furthermore, the surface energy term can be of higher magnitude for nano-sized particles, as compared to that normally assumed for a flat surface, which would result in further impetus to the developed internal pressure.[31] It must be mentioned here that in an earlier study, stabilization of high-pressure modification phase (monoclinic) in nanocrystalline yttria has also been attributed to the aforementioned GT effect.[31,32]

Therefore, we believe that the synergistic effects of the constraining pressure (due to coefficient of thermal expansion mismatch with WC) and nanocrystallinity of

TABLE II. Values of parameters used to calculate pressure due to thermal expansion mismatch.

Parameter	Value
α_{ZrO_2} (linear thermal expansion coefficient of ZrO_2)	11×10^{-6} K^{-1}
α_{WC} (linear thermal expansion coefficient of WC)	5.2×10^{-6} K^{-1}
ΔT	(1400 + 273) – 300 = 1373 K
μ_{WC}	262 GPa
K_{ZrO_2}	150.6 GPa

ZrO_2 may be sufficient to effect a transformation to the high-pressure modification (o-ZrO_2) in spark sintered WC-ZrO_2 nanocomposites. This is corroborated by the report of the formation of o-ZrO_2 during high pressure experiment[33] as well as during internal oxidation of Cu-Zr alloy.[34]

Regarding the formation of W_2C, our observations of the presence of W_2C between the WC and ZrO_2 grains [Fig. 6(a)] suggest the occurrence of a possible reaction between WC and ZrO_2 at the interface[27]:

$$ZrO_{2-x} + 2yWC = yW_2C + ZrO_{2-x-y} + yCO \quad , \tag{3}$$

where x is the oxygen vacancy concentration in the ZrO_2 as a result of the dopant concentration, and y is the additional vacancy concentration created in the ZrO_2 due to reaction with WC.

On the basis of the microstructural observations, it is possible to develop insight into the mechanism of sintering and the role of ZrO_2 in achieving high sinter density of WC at significantly lower temperature. As has been reported earlier,[23,24] the densification of binderless WC over 98% ρ_{th} requires a substantially higher temperature of 1700 °C in spark plasma sintering route. Thus, the presence of ZrO_2 clearly plays a dominant role during spark plasma sintering of the nanocomposites at 1300 °C. This can be correlated with the occurrence of reaction between WC and ZrO_2 [Eq. (3)]. Such a reaction creates (i) additional oxygen vacancies and (ii) formation of a layer of W_2C. The availability of additional oxygen vacancies results in enhanced non-stoichiometry of the ZrO_2 phase. This may enhance the diffusivity to a certain extent, resulting in faster mass transport and hence increased sintering kinetics.

Following critical observations of TEM images (see Fig. 2), another plausible reason for the enhancement of densification rate of WC in the presence of ZrO_2 can be put forward. A significant fraction of the nanocrystalline ZrO_2 particles is found to be present along the WC grain boundaries. These intergranular zirconia particles can potentially restrict the matrix grain boundary mobility during sintering. Such a pinning effect due to ZrO_2 particles can prevent considerable grain growth of the WC during spark sintering at 1300 °C.

It has also been reported by Cha et al.[23] that the presence of carbon enhances abnormal grain growth in binderless WC by the SPS process. The addition of carbon increases the driving force for grain growth. We believe that the formation of W_2C, during spark sintering of our WC-ZrO_2 nanocomposite leads to a depletion of carbon content in the neighboring WC grains. This suggests that W_2C formation contributes toward a decrease in boundary mobility and thereby hindering the grain growth of WC. The relative absence of grain growth can also be confirmed from finer size distribution of WC grains [see Fig. 2(a)]. The retention of finer crystallite size of matrix WC would lead to an enhancement of sintering kinetics due to augmentation of the sintering driving force. It can be recalled here that the sintering time follows a direct power law relationship with particle size (Herring's scaling law). Earlier research also demonstrated the lowering of sintering temperature for finer WC particles.[35] Therefore, based on the established sintering theory, it can be expected that finer particle assembly would densify faster at lower temperature.

The influence of ZrO_2 in enhancing sintering kinetics can also be related to size effect. The dispersed nano-sized ZrO_2 possess higher specific surface area. This, in turn, results in increased volume fraction of the interfacial area. Because grain boundaries provide faster diffusion paths, the accretion of grain boundary area can lead to faster mass transport. Such an effect of nano-sized dispersoids in lowering sintering temperature has also been reported in a recent research publication.[36]

During SPS, the conduction of electrical current through a collection of powder is governed by a phenomenon known as constriction resistance when there is a small contact area compared to the dimensions of the powder particles. The nanocrystalline ZrO_2 particles give rise to higher "constriction resistance" (R_c) due to their ultrafine size, leading to smaller particle-to-particle contact area and higher resistivity, according to the equation[37]:

$$R_C(n,a,l) = \frac{\rho f_s}{2\pi n a} \arctan\left(\frac{\sqrt{l^2 - a^2}}{a}\right) \quad , \tag{4}$$

where a is the linear dimension of the interparticle contact, ρ is the resistivity of the powder, l is the nearest distance between the contacts, and f_s is a shape factor. Therefore, voltage drop takes place over a small distance around the contact area of the nanoparticles, and a localized area of high resistance is formed with a very high joule heating. This leads to local increase in temperature. It is to be noted that the volume fraction of ZrO_2 is ~14% and that the ZrO_2 particles are well dispersed in the WC matrix [Fig. 2(a)]. The presence of this considerable amount of zirconia can effectively result in a local increase in temperature around a number of WC/ZrO_2 interfaces. From the fundamental sintering theory, the higher the temperature in the neck region is, the faster the mass transport will be. Such a phenomenon leads to an enhancement of mass flow rate with concomitant augmentation of necking and hence resultant sintering kinetics.

We note that no evidence of any residue of sintering liquid could be found from the microstructural analysis. This confirms that the use of ZrO_2 sinter-additive results in solid-state sintering of the WC matrix. This is in

contrast to liquid phase sintering, which enhances densification of WC-Co cermets. Our results indicate that the SPS process enables the full densification of WC-Co at temperatures about 100 °C lower than the pressureless sintering temperature whereas WC-ZrO_2 can be densified to near theoretical density at a temperature 400 °C lower than that under pressureless sintering conditions.

V. CONCLUSIONS

In the present work, we investigated the processing and microstructural development in WC-ZrO_2 nanocomposites, sintered via SPS. Based on the analysis of the obtained experimental results, the following major conclusions can be made.

(1) WC–6 wt% ZrO_2 nanocomposites with near-theoretical density can be obtained via the spark sintering route at a relatively lower sintering temperature of 1300 °C and little holding time of 5 min. Such results prove the superiority of SPS in achieving faster densification of WC-ZrO_2 composites, compared to the pressureless sintering route (1700 °C, 1 h). The presence of non-stoichiometric nanocrystalline ZrO_2, resulting in faster mass transport, was identified as one of the reasons for enhanced densification in the presence of ZrO_2.

(2) As indicated by XRD results, detectable amounts of W_2C form during SPS with holding times of 5 min or more. W_2C formation occurred during sintering as a result of the sintering reaction between WC and ZrO_2.

(3) TEM analysis revealed the dispersion of nano-sized ZrO_2 particles, present at the WC grain boundaries, grain boundary triple points, and also within the grains. The ZrO_2 present within the WC grains was relatively finer in size (30–50 nm) than the intergranular particles (60–100 nm). Such characteristic presence of nano-sized ZrO_2 reinforcements enabled the developed composite to be called "inter/intragranular ceramic nanocomposites."

(4) An interesting observation was the presence of ZrO_2 in its orthorhombic crystal structure. The evidence for this is recorded in both sintered sample (XRD result) as well as on thin foil (TEM analysis) of the spark plasma sintered nanocomposite. The large residual stress, induced by thermal expansion anisotropy, generated during high temperature exposure of the WC-ZrO_2 nanocomposites, coupled with nano-size effects, appears to have caused the t-ZrO_2 to o-ZrO_2 transformation during spark sintering.

ACKNOWLEDGMENT

The use of the SPS facility available at Sintering and Microstructure Laboratory, Creative Research Centre, School of Materials Research Centre, School of Material Science, Seoul National University, South Korea is gratefully acknowledged.

REFERENCES

1. B. Basu, J.H. Lee, and D.Y. Kim: Development of WC-ZrO_2 nanocomposites by spark plasma sintering. *J. Am. Ceram. Soc.* **87,** 317 (2004).
2. M. Sternitzke: Review: Structural ceramic nanocomposites. *J. Eur. Ceram. Soc.* **17,** 1061 (1997).
3. R.D. Shull: View point: Nanocrystalline and nano phase materials. *Nanostruct. Mater.* **2,** 213 (1993).
4. R.S. Averbek, H.J. Holfer, and R. Tao: Processing of nanograined materials. *Mater. Sci. Eng., A* **66,** 169 (1993).
5. S. Komarneni: Nanocomposites. *J. Mater. Chem.* **2,** 1219 (1992).
6. C. Suryanarayana: Nanocrystalline materials. *Int. Mater. Rev.* **40,** 41 (1995).
7. H. Gleiter: Nanostructured materials: State of the art and perspectives. *Z. Metallkd.* **86,** 78 (1995).
8. T. Kusunose, T. Sekino, Y.H. Choa, and K. Niihara: Machinability of silicon nitride/boron nitride nanocomposites. *J. Am. Ceram. Soc.* **85,** 2689 (2002).
9. K. Niihara: New design concept of structural ceramics-ceramic nano composites. *J. Ceram. Soc. Jpn. The Centennial Memorial Issue* **99,** 974 (1991).
10. L. Gao, H.Z. Wang, J.S. Hong, H. Miyamoto, K. Miyamoto, Y. Nishikawa, and S.D.D.L. Torre: SiC–ZrO_2(3Y)–Al_2O_3 nanocomposites superfast densified by spark plasma sintering. *Nanostruct. Mater.* **11,** 43 (1999).
11. L. Gao, X. Jin, H. Kawaoka, T. Sekino, and K. Niihara: Microstructure and mechanical properties of SiC-mullite nanocomposite prepared by spark plasma sintering. *Mater. Sci. Eng., A* **334,** 262 (2002).
12. B. Basu, T. Venkateswaran, and D.Y. Kim: Microstructure and properties of spark plasma sintered ZrO_2–ZrB_2 nanoceramic composites. *J. Am. Ceram. Soc.* **89,** 2405 (2006).
13. D.S. Perara, M. Tokita, and S. Moricca: Comparative study of fabrication of Si_3N_4/ SiC composites by spark plasma sintering and hot isostatic pressing. *J. Eur. Ceram. Soc.* **18,** 401 (1998).
14. L. Gao, H.Z. Wang, J.S. Hong, H. Miyamoto, K. Miyamoto, Y. Nishikawa, and S.D.D.L. Torre: Mechanical properties and microstructure of nano-SiC–Al_2O_3 composites densified by spark plasma sintering. *J. Eur. Ceram. Soc.* **19,** 609 (1999).
15. G.D. Zhan, J. Kuntz, J. Wan, J. Garay, and A.K. Mukherjee: Spark-plasma-sintered $BaTiO_3$/Al_2O_3 nanocomposites. *Mater. Sci. Eng., A* **356,** 443 (2003).
16. J.R. Groza, *ASM Materials Handbook,* Vol. 7 (ASM International, Materials Park, OH, 1998), p. 583.
17. Z.A. Munir and U.A. Tamburini: The effect of electric field and pressure on the synthesis and consolidation of materials: A review of the spark plasma sintering method. *J. Mater. Sci., A* **41,** 763 (2006).
18. B. Basu, T. Venkateswaran, and D. Sarkar: Pressureless sintering and tribological properties of WC-ZrO_2 composites. *J. Eur. Ceram. Soc.* **25,** 1603 (2005).
19. T. Venkateswaran, D. Sarkar, and B. Basu: Tribological properties of WC-ZrO_2 nanocomposites. *J. Am. Ceram. Soc.* **88,** 691 (2005).
20. R. Suyama, T. Shida, and S. Kume: Synthesis of the orthorhombic phase of ZrO_2. *J. Am. Ceram. Soc.* **68,** C314 (1985).
21. O. Ohtaka, S. Kume, and T. Iwami: Synthesis of the orthorhombic phase of 2Y-ZrO_2. *J. Am. Ceram. Soc.* **71,** C164 (1988).
22. D.B. Marshall, M.R. James, and J.R. Porter: Structural and mechanical property change in toughened Mg-PSZ at low temperature. *J. Am. Ceram. Soc.* **72,** 218 (1989).
23. S.I. Cha and S.H. Hong: Microstructures of binderless tungsten carbides sintered by spark plasma sintering process. *Mater. Sci. Eng., A* **356,** 381 (2003).
24. M. Omori: Sintering, consolidation, reaction and crystal growth

by the spark plasma system (SPS). *Mater. Sci. Eng., A* **287,** 183 (2000).
25. E.H. Kisi, C.J. Howard, and R.J. Hill: Crystal structure of orthorhombic zirconia in partially stabilized zirconia. *J. Am. Ceram. Soc.* **72,** 1757 (1989).
26. R. Guinebretière, Z. Oudjedi, and A. Dauger: Orthorhombic zirconia phase in ZrO_2–$MgAl_2O_4$ composite materials. *Scripta Mater.* **34,** 1039 (1996).
27. Z. Pedzich: The reliability of particulate composites in the TZP/WC system. *J. Eur. Ceram. Soc.* **24,** 3427 (2004).
28. N. Moskala and W. Pyda: Thermal stability of tungsten carbide in 7 mol% calcia–zirconia solid solution matrix heat treated in argon. *J. Eur. Ceram. Soc.* (2006, in press).
29. A.H. Heuer, R. Chaim, and V. Lanteri: Review: Phase transformations and microstructural characterization of alloys in the system Y_2O_3-ZrO_2, in *Advances in Ceramics*, Vol. 24A, edited by: S. Somiya, N. Yamamoto, and H. Yanagida.
30. F. Spaepen and D. Turnbull: Negative pressures and melting point depression in oxide coated liquid metal droplets. *Scripta Metall.* **13,** 149 (1979).
31. G. Skandan, C.M. Foster, H. Frase, M.N. Ali, J.C. Parker, and H. Hahn: Phase characterization and stabilization due to grain size effects of nanostructured Y_2O_3. *Nanostruct. Mater.* **1,** 313 (1992).
32. H. Hahn: Microstructure and properties of nanostructured oxides. *Nanostruct. Mater.* **2,** 251 (1993).
33. N.A. Bendeliyani, S.V. Popova, and L.F. Veraschagin: New high pressure phases of ZrO_2 and HfO_2. *Geokhimya* **6,** 677 (1967).
34. Y.H. Chiao and I-W. Chen: Grain boundary structure and related phenomena. *Trans. Jpn. Inst. Metals. Proc. of JIMIS, No. 4,* **27**(Suppl.), 197 (1986).
35. S. Imasato, K. Tokumoto, T. Kitada, and S. Sakaguchi: Properties of ultra-fine grain binderless cemented carbide 'RCCFN'. *Int. J. Refract. Met. Hard Mater.* **13,** 305 (1995).
36. H. Liu, C. Huang, J. Wang, and X. Teng: Fabrication and mechanical properties of Al_2O_3/Ti($C_{0.7}N_{0.3}$) nanocomposites. *Mater. Res. Bull.* **41,** 1215 (2006).
37. Holm: *Electric Contacts: Theory and Applications,* 4th ed. (Springer, New York, 1967).